Proceedings of the 10th Brazilian Congress of Thermal Sciences and Engineering -- ENCIT 2004
Braz. Soc. of Mechanical Sciences and Engineering -- ABCM, Rio de Janeiro, Brazil, Nov. 29 -- Dec. 03, 2004

Paper CIT04-0630

NUMERICAL SIMULATION OF THE LAMINAR TRANSONIC BUFFET IN A TWO-DIMENSIONAL BASE

Roberto F. Bobenrieth Miserda
Universidade de Brasília, ENM – FT – UnB, Campus Universitário, Asa Norte, Brasília, DF, 70910-900, Brasília, DF, Brasil
rfbm@unb.br

Alessandra Freire de Mendonça
Universidade de Brasília, ENM – FT – UnB, Campus Universitário, Asa Norte, Brasília, DF, 70910-900, Brasília, DF, Brasil
afmend@engineer.com

Abstract. *The objective of this work is the numerical simulation of the vortex-shock interactions that appears in the transonic regime for the laminar flow in a two-dimensional base. The compressible Navier-Stokes equations are numerically solved using a finite volume discretization in combination with the skew-symmetric form of Ducros' fourth-order numerical scheme. Results are obtained for Mach numbers ranging from 0.80 to 1.05 for a Reynolds number of 1,000. For subsonic Mach numbers, the visualization shows the acoustics waves generated by the boundary layers along the side walls and their progressive accumulation until their coalescence into a shock at supersonic Mach numbers. Also, the analysis of the visualizations shows a strong variation in the type of the vortex-shock interactions over the transonic range. For a Mach number of 1.05, the buffet phenomenon disappears, giving place to a steady recirculation region and trailing wake in contact with a steady expansion-compression wave system.*

Keywords*. Two-dimensional base, transonic buffet, laminar flow, compressible flow.*

1. Introduction

This work is aimed at the numerical simulation of the strong vortex-shock interaction that arises in the transonic flow over a two-dimensional base in laminar regime. This kind of interaction is the cornerstone of the transonic-buffet phenomenon, of high interest in the aerospace sciences. Due to the complex nature of the vortex-shock interaction, not every numerical method is able to tackle this type of problems. Only shock-capturing schemes can obtain meaningful results. One drawback of this type of methods is the tendency to over dissipate in regions that are not shock waves, such as high shear-stress regions, resulting in the dumping of the phenomenon. In this work, a new type of sensor, proposed by Ducros et al. (1999) is used for appropriately trigging the artificial dissipation in order to minimize this problem.

The numerical simulation of vortex-shock interactions has been the focus of many recent works. Yee et al. (1999) proposed a family of low-dissipative and high-orders shock-capturing methods using characteristic-based filters to minimize the numerical dissipation of the overall scheme. This methodology was successfully applied to the simulation of the vortex pairing in a time-developing laminar mixing layer, the shock-wave impingement on a spatially evolving laminar mixing layer and a compressible turbulent channel flow. The former two problems were also solved by Yee et al. (2000) using an entropy-splitting approach. This approach was also used by Sandham et al. (2002) in the numerical simulation of the compressible channel flow. The idea of a skew-symmetric splitting was presented by Yee and Sjogreen (2001) and used to simulate the complex two-dimensional shock/boundary-layer interaction in the laminar problem proposed by Daru and Tenaud (2001). All the above works used a finite-difference discretization. Ducros et al. (2000) proposed a family of high-order fluxes for conservative skew-symmetric-like schemes using structured meshes that can be used by a finite-difference or a finite-volume discretization. In this work, Ducros' fourth-order skew-symmetric scheme for a finite-volume discretization in conjunction with a third-order Runge-Kutta time-marching method is used. The resulting numerical scheme is fourth-order accurate in space and third-order accurate in time.

2. Mathematical Model

The nondimensional form of the compressible Navier-Stokes equations can be written as:

$$\frac{\partial \rho}{\partial t} + \frac{\partial}{\partial x_i}(\rho u_i) = 0 , \tag{1}$$

$$\frac{\partial}{\partial t}(\rho u_i) + \frac{\partial}{\partial x_j}(\rho u_i u_j) = -\frac{\partial p}{\partial x_i} + \frac{\partial \tau_{ij}}{\partial x_j} , \tag{2}$$

$$\frac{\partial}{\partial t}(\rho e_T) + \frac{\partial}{\partial x_i}(\rho e_T u_i) = -\frac{\partial}{\partial x_i}(p u_i) + \frac{\partial}{\partial x_i}(\tau_{ij} u_j) - \frac{\partial q_{x_i}}{\partial x_i} . \tag{3}$$

All the variables are in nondimensional form and have their usual meaning, i.e., x_i is the *i*-direction spatial coordinate, t is the temporal coordinate, r is the density, u_i is the *i*-direction component of the velocity vector, p is the thermodynamic pressure, T is the temperature, e is the internal specific energy, m is the viscosity, c_v is the specific heat at constant volume, t_{ij} is the viscous stress tensor, e_T is the total specific energy and q_{x_i} is *i*-direction of the heat-flow density vector. The nondimensional form for all the variables is defined using the following procedure:

$$x_i = \frac{x_i^*}{L^*}, \quad u_i = \frac{u_i^*}{U_\infty^*}, \quad t = \frac{t^*}{L^*/U_\infty^*}, \quad p = \frac{p^*}{r_\infty^*\left(U_\infty^*\right)^2}, \quad r = \frac{r^*}{r_\infty^*}, \quad T = \frac{T^*}{T_\infty^*}, \quad e = \frac{e^*}{\left(U_\infty^*\right)^2}, \quad m = \frac{m^*}{m_\infty^*}, \quad c_v = \left[\frac{T_\infty^*}{\left(U_\infty^*\right)^2}\right]c_v^*, \tag{4}$$

where U_∞^* is the velocity magnitude of the undisturbed flow, L^* is the characteristic length of the problem, the superscript * represents dimensional variables and the subscript ∞ stands for undisturbed-flow properties.

The viscous-stress tensor is given by

$$t_{ij} = \frac{1}{\mathrm{Re}}\left(m\, S_{ij}\right) = \frac{1}{\mathrm{Re}}\left\{m\left[\left(\frac{\partial u_i}{\partial x_j} + \frac{\partial u_j}{\partial x_i}\right) - \frac{2}{3}d_{ij}\frac{\partial u_k}{\partial x_k}\right]\right\}, \tag{5}$$

where S_{ij} is the nondimensional rate-of-strain tensor, d_{ij} is the Kronecker delta and the Reynolds number is defined as

$$\mathrm{Re} = \frac{r_\infty^* U_\infty^* L^*}{m_\infty^*}. \tag{6}$$

The total energy is given by the sum of the internal and kinetic specific energy as

$$e_T = e + e_k = c_v T + \frac{u_i u_i}{2}, \tag{7}$$

and the heat-flux density is

$$q_{x_i} = -\frac{m}{(g-1)M^2\,\mathrm{Re}\,\mathrm{Pr}}\left(\frac{\partial T}{\partial x_i}\right), \tag{8}$$

where g is the specific-heat ratio and the Mach and Prandtl numbers are respectively defined as

$$M = \frac{U_\infty^*}{\sqrt{g\,R^*\,T_\infty^*}}, \qquad \mathrm{Pr} = \frac{c_p^*}{k_\infty^*}m_\infty^*. \tag{9}$$

In this work, the Prandtl number is considered a constant with the value $\mathrm{Pr} = 0.72$. For a thermally and calorically perfect gas, the nondimensional equation of state can be written as

$$p = (g-1)re \tag{10}$$

and

$$T = \frac{g\,M^2 p}{r}. \tag{11}$$

The nondimensional molecular viscosity is obtained using Sutherland's formula

$$m = C_1\frac{T^{3/2}}{T + C_2}, \qquad C_1 = \left[\frac{\left(T_\infty^*\right)^{1/2}}{m_\infty^*}\right]C_1^*, \qquad C_2 = \frac{C_2^*}{T_\infty^*}, \tag{12}$$

where C_1^* and C_2^* are dimensional constants.

The boundary conditions at the wall of the two-dimensional base are a no-slip condition for the velocity field, an adiabatic wall for the temperature field and a null gradient in the normal direction at the wall for the pressure field.

3. Numerical Method

Since the geometry of interest is a two-dimensional base and the flow around it is laminar, the two-dimensional form of the Navier-Stokes is used. In order to numerically solve this equations using a finite volume approach, Eqs. (1), (2) and (3) are written in the following vector form (Anderson et al., 1983):

$$\frac{\partial \mathbf{U}}{\partial t}+\frac{\partial \mathbf{E}}{\partial x}+\frac{\partial \mathbf{F}}{\partial y}=\mathbf{0}, \tag{13}$$

where the conservative-variables vector **U**, and the flux vectors **E** and **F** are given by

$$\mathbf{U}=\begin{bmatrix} \rho \\ \rho u \\ \rho v \\ \rho e_T \end{bmatrix}, \quad \mathbf{E}=\begin{bmatrix} \rho u \\ \rho u^2+p-\tau_{xx} \\ \rho uv-\tau_{xy} \\ (\rho e_T+p)u-u\tau_{xx}-v\tau_{xy}+q_x \end{bmatrix}, \quad \mathbf{F}=\begin{bmatrix} \rho v \\ \rho vu-\tau_{xy} \\ \rho v^2+p-\tau_{yy} \\ (\rho e_T+p)v-u\tau_{xy}-v\tau_{yy}+q_y \end{bmatrix}. \tag{14}$$

Defining the flux tensor Π as

$$\Pi=\mathbf{E}\otimes\mathbf{i}+\mathbf{F}\otimes\mathbf{j}, \tag{15}$$

where $\mathbf{i}$ and $\mathbf{j}$ are the unit vectors in the *x* and *y*-direction, Eq. (13) can be rewritten as

$$\frac{\partial \mathbf{U}}{\partial t}+\nabla\cdot\Pi=0. \tag{16}$$

Integrating the above equation over the control volume *V*, and applying the divergence theorem to the right-hand side results

$$\frac{\partial}{\partial t}\int_V \mathbf{U}\,dV=-\int_V(\nabla\cdot\Pi)dV=-\int_S(\Pi\cdot\mathbf{n})dS, \tag{17}$$

where *S* is the control surface that defines the control volume. Defining the volumetric mean of the vector **U** in the control volume *V* as

$$\overline{\mathbf{U}}\equiv\frac{1}{V}\int_V \mathbf{U}\,dV, \tag{18}$$

Eq. (17) is written as

$$\frac{\partial \overline{\mathbf{U}}}{\partial t}=-\frac{1}{V}\int_S(\Pi\cdot\mathbf{n})dS, \tag{19}$$

where $\mathbf{n}$ is the unit vector normal to the surface *S*.

For the volume (i, j), the first-order approximation of the temporal derivative is given by

$$\left(\frac{\partial \overline{\mathbf{U}}}{\partial t}\right)_{i,j}=\frac{\Delta\overline{\mathbf{U}}_{i,j}}{\Delta t}+O(\Delta t), \tag{20}$$

and the temporal approximation of Eq. (19) for a quadrilateral and two-dimensional control volume is

$$\Delta\overline{\mathbf{U}}_{i,j} = -\frac{\Delta t}{V_{i,j}}\left[\int_{S_{i+1/2}}(\Pi\cdot\mathbf{n})dS + \int_{S_{i-1/2}}(\Pi\cdot\mathbf{n})dS + \int_{S_{j+1/2}}(\Pi\cdot\mathbf{n})dS + \int_{S_{j-1/2}}(\Pi\cdot\mathbf{n})dS\right], \tag{21}$$

where $S_{i+1/2}$ is the common surface between volume (i, j) and volume $(i+1, j)$. Defining the function of the flux of tensor Π over the control surface *S* as

$$F\left(\overline{\mathbf{U}}\right)_{i,j} = \frac{\Delta t}{V_{i,j}}\left[(\Pi\cdot\mathbf{S})_{i+1/2} + (\Pi\cdot\mathbf{S})_{i-1/2} + (\Pi\cdot\mathbf{S})_{j+1/2} + (\Pi\cdot\mathbf{S})_{j-1/2}\right], \tag{22}$$

the spatial approximation of Eq. (21) is

$$\Delta\overline{\mathbf{U}}_{i,j} = -\left[F\left(\overline{\mathbf{U}}\right)_{i,j} - D\left(\overline{\mathbf{U}}\right)_{i,j}\right], \tag{23}$$

where $D\left(\overline{\mathbf{U}}\right)_{i,j}$ is an artificial dissipation. It is important to note that Eq. (23) is a spatial approximation of Eq. (21) because tensor Π is considered constant over each of the four control surfaces that define the control volume.

In order to calculate $F\left(\overline{\mathbf{U}}\right)_{i,j}$, the flux of tensor Π trough the control surfaces must be calculated. For the surface $\mathbf{S}_{i+1/2}$, this flux is given by

$$(\Pi\cdot\mathbf{S})_{i+1/2} = \begin{bmatrix} r_{i+1/2}(q_S)_{i+1/2} \\ (ru)_{i+1/2}(q_S)_{i+1/2} + p_{i+1/2}(s_x)_{i+1/2} - \left[m_{i+1/2}(S_{xx})_{i+1/2}\right](s_x)_{i+1/2} - \left[m_{i+1/2}(S_{xy})_{i+1/2}\right](s_y)_{i+1/2} \\ (rv)_{i+1/2}(q_S)_{i+1/2} + p_{i+1/2}(s_y)_{i+1/2} - \left[m_{i+1/2}(S_{xy})_{i+1/2}\right](s_x)_{i+1/2} - \left[m_{i+1/2}(S_{yy})_{i+1/2}\right](s_y)_{i+1/2} \\ (r\,e_T)_{i+1/2}(q_S)_{i+1/2} + p_{i+1/2}(q_S)_{i+1/2} - u_{i+1/2}(s_x)_{i+1/2}\left[m_{i+1/2}(S_{xx})_{i+1/2}\right] - v_{i+1/2}(s_y)_{i+1/2}\left[m_{i+1/2}(S_{yy})_{i+1/2}\right] \\ \qquad - \left[v_{i+1/2}(s_x)_{i+1/2} + u_{i+1/2}(s_y)_{i+1/2}\right]\left[m_{i+1/2}(S_{xy})_{i+1/2}\right] \\ \qquad - \left[k_{i+1/2}(\partial T/\partial x)_{i+1/2}\right](s_x)_{i+1/2} - \left[k_{i+1/2}(\partial T/\partial y)_{i+1/2}\right](s_y)_{i+1/2} \end{bmatrix}. \tag{24}$$

where the volumetric flux $(q_S)_{i+1/2}$ is defined by

$$(q_S)_{i+1/2} = \mathbf{u}_{i+1/2}\cdot\mathbf{S}_{i+1/2} = u_{i+1/2}(s_x)_{i+1/2} + v_{i+1/2}(s_y)_{i+1/2}, \tag{25}$$

where $\mathbf{u}$ is the velocity vector.

It is important to note that the first terms in the right-hand side of Eq. (24) are the fluxes of mass, momentum and total energy through surface $\mathbf{S}_{i+1/2}$ and the other terms represents the fonts of variation of momentum and total energy. In order to evaluate all this terms, in this work is used the fourth-order skew-symmetric scheme proposed by Ducros et al. (2000) given by

$$u_{i+1/2} = \frac{2}{3}\left(\underline{u}_i + \underline{u}_{i+1}\right) - \frac{1}{12}\left(\underline{u}_{i-1} + \underline{u}_i + \underline{u}_{i+1} + \underline{u}_{i+2}\right), \tag{26}$$

and

$$\begin{aligned}(ru)_{i+1/2} \equiv{}& \frac{1}{3}\left(\overline{r}_i + \overline{r}_{i+1}\right)\left(\underline{u}_i + \underline{u}_{i+1}\right) \\ & - \frac{1}{24}\left(\overline{r}_{i-1}\underline{u}_{i-1} + \overline{r}_{i+1}\underline{u}_{i-1} + \overline{r}_i\underline{u}_i + \overline{r}_{i+2}\underline{u}_i + \overline{r}_{i+1}\underline{u}_{i+1}\right. \\ & \qquad \left. + \overline{r}_{i-1}\underline{u}_{i+1} + \overline{r}_{i+2}\underline{u}_{i+2} + \overline{r}_i\underline{u}_{i+2}\right) \\ & + \frac{1}{3}\left[\frac{1}{2}\left(\overline{r}_{i+1}\underline{u}_{i+1} + \overline{r}_i\underline{u}_i\right) - \frac{1}{4}\left(\overline{r}_{i+1} + \overline{r}_i\right)\left(\underline{u}_{i+1} + \underline{u}_i\right)\right],\end{aligned} \tag{27}$$

since all calculated properties in the right-hand side of Eqs. (26) and (27) are volumetric means centered at the volume. The over bar indicates the volumetric mean defined by Eq. (19) and the under bar refers to the Favre mean, defined as

$$\underline{u} = \frac{\overline{ru}}{\overline{r}} . \tag{28}$$

The scheme proposed by Eqs. (27) and (28) is a centered one, and therefore, an explicit artificial viscosity must be included in Eq. (24). In order to enhance the numerical method with shock-capturing capabilities and the ability to cope with steep gradient regions, this artificial dissipation uses the basic idea proposed by Jameson et al. (1981) given by

$$D(\overline{\mathbf{U}}) = \left[d_{i+1/2}(\overline{\mathbf{U}}) - d_{i-1/2}(\overline{\mathbf{U}})\right] + \left[d_{j+1/2}(\overline{\mathbf{U}}) - d_{j-1/2}(\overline{\mathbf{U}})\right] , \tag{29}$$

where

$$d_{i+1/2}(\overline{\mathbf{U}}) = e^{(2)}_{i+1/2}\left[(\overline{\mathbf{U}})_{i+1} - (\overline{\mathbf{U}})_i\right] - e^{(4)}_{i+1/2}\left[(\overline{\mathbf{U}})_{i+2} - 3(\overline{\mathbf{U}})_{i+1} + 3(\overline{\mathbf{U}})_i - (\overline{\mathbf{U}})_{i-1}\right]. \tag{30}$$

The first and second terms of Eq. (30) are a second-order and a fourth-order dissipation, respectively. The first term acts in the shock and the second term acts over steep gradient regions, like the viscous regions. The coefficients of Eq. (30) are given by

$$e^{(2)}_{i+1/2} = k^{(2)}\max(\Psi_i\Phi_i, \Psi_{i+1}\Phi_{i+1}), \quad e^{(4)}_{i+1/2} = \max\left[0, \left(k^{(4)} - e^{(2)}_{i+1/2}\right)\right], \quad k^{(2)} = 1/4, \quad k^{(4)} = 1/256 , \tag{31}$$

where the sensors Ψ_i and Φ_i are

$$\Psi_i = \frac{\left|\overline{p}_{i+1} - 2\overline{p}_i + \overline{p}_{i-1}\right|}{\left|\overline{p}_{i+1}\right| + \left|2\overline{p}_i\right| + \left|\overline{p}_{i-1}\right|}, \quad \Phi_i = \frac{(\nabla\cdot\underline{\mathbf{u}})^2}{(\nabla\cdot\underline{\mathbf{u}})^2 + \left|\nabla\times\underline{\mathbf{u}}\right|^2 + e}, \quad e = 10^{-30} . \tag{32}$$

The sensor Ψ_i is pressure-based and it is intended to detect the shock waves. The sensor Φ_i was proposed by Ducros et al. (1999), and its function is to inhibit sensor Ψ_i in regions were the divergent is low, but the rotational of the velocity field is high, like a pure vortex wake. In regions were the divergent and the rotational are high, like the vortex-shock interaction, the inhibiting capacity of sensor Φ_i decreases.

In order to advance Eq. (24) in time, a third-order Runge-Kutta is used as proposed by Shu (Yee, 1997). This yield to

$$\begin{aligned}
\overline{\mathbf{U}}^1 &= \overline{\mathbf{U}}^n - \left[F(\overline{\mathbf{U}}^n) - D(\overline{\mathbf{U}}^n)\right] \\
\overline{\mathbf{U}}^2 &= \frac{3}{4}\overline{\mathbf{U}}^n + \frac{1}{4}\overline{\mathbf{U}}^1 - \frac{1}{4}\left[F(\overline{\mathbf{U}}^1) - D(\overline{\mathbf{U}}^1)\right] \\
\overline{\mathbf{U}}^{n+1} &= \frac{1}{3}\overline{\mathbf{U}}^n + \frac{2}{3}\overline{\mathbf{U}}^2 - \frac{2}{3}\left[F(\overline{\mathbf{U}}^2) - D(\overline{\mathbf{U}}^2)\right]
\end{aligned} \tag{33}$$

As proposed in this work, the resulting numerical method is fourth-order accurate in space and third-order accurate in time.

4. Results

For all the cases studied in this work the Reynolds number is 1,000, and the characteristic length L^* is the base thickness. The Mach number ranges from 0.80 to 1.05. The base thickness is discretized by 30 control volumes. The regular region of the computational grid after the expansion is $35L^*$ in height and $17L^*$ in length. Before the expansion, the regular region of the computational grid is $17L^*$ in height and $4L^*$ in length, both in the upper and lower side of the two-dimensional base. In conjunction with the stretched regions of the grid, the total number of control volumes is 803,700 resulting in a problem with 3,214,800 degrees of freedom.

Figure 1 shows only the regular region of the computational domain in conjunction with a zoom showing the regular resolution of the computational grid. It is important to recall that the fourth-order accuracy in space of the numerical scheme applies only to the regular region of the grid (Ref. 3). The variable plotted is the nondimensional magnitude of the temperature gradient. White corresponds to 0.0 and black corresponds to 1.5. The Mach number is 0.9. A very strong vortex-shock interaction is observed.

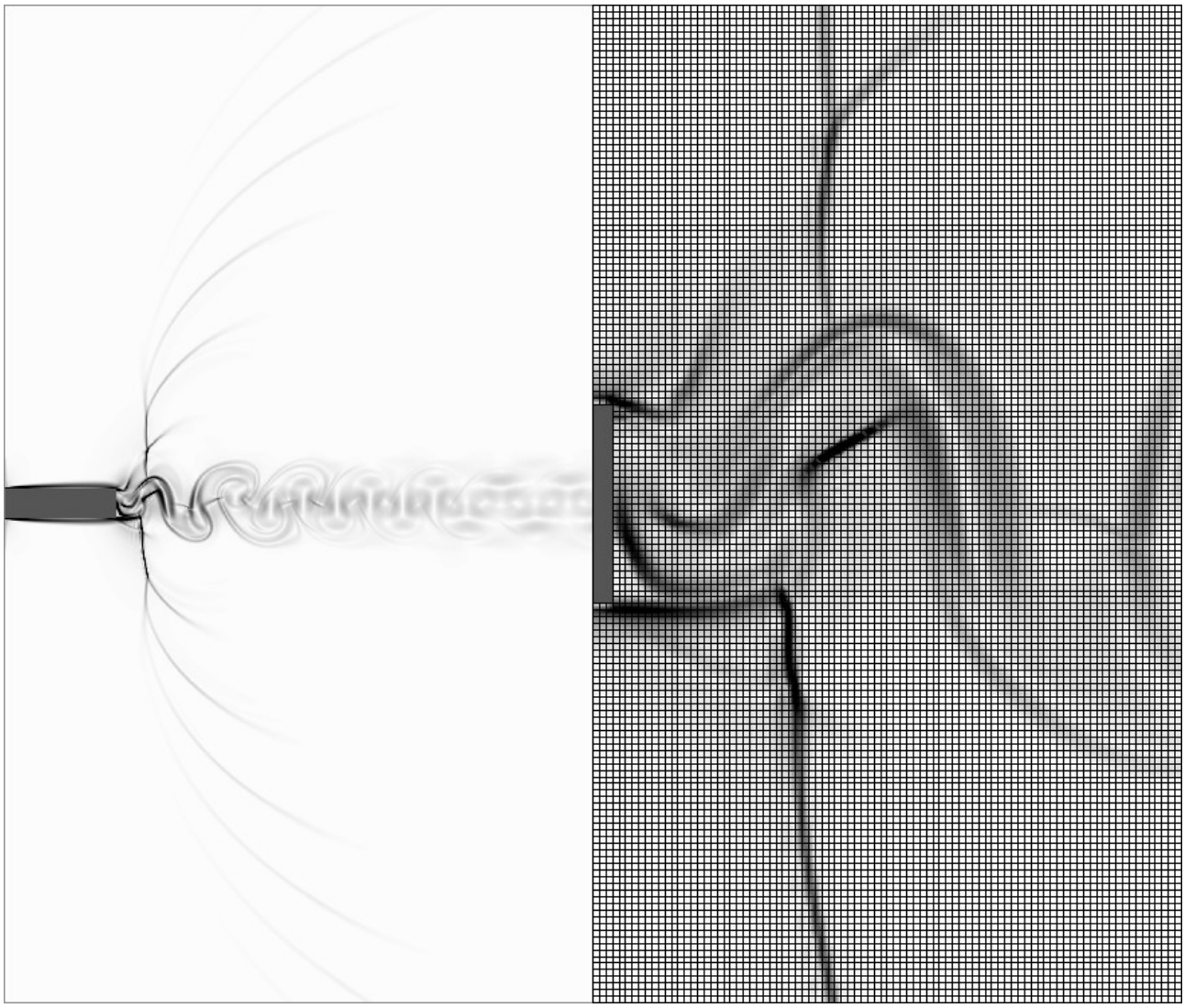

Figure 1. Region of regular resolution of the computational grid and zoom of grid resolution.

4.1. M=0.80

From the visualization presented in Fig. 2 it can be seen that the unsteady Vón Kármán vortex street is well defined and a coalescence of vortices is visible at the end of the left side of the figure. This coalescence is also associated with a very strong acoustic wave that is positioned in middle of the vortex wake and moving upstream. In the zoom, it is also possible to clearly see the formation of a lambda shock associated with the separation of the boundary layer in the upper-right corner of the base. This lambda shock separates from the detached vortex and travels as a strong acoustic wave in a direction that is basically normal to the incoming flow. In the zoom it is also possible to note that a connecting shock appears between the detached vortices. The intensity of this shock decreases rapidly as the vortices move in the downstream direction. The variable plotted is the nondimensional magnitude of the temperature gradient. White corresponds to 0.0 in both parts and black corresponds to 1.0 (left part) and to 2.0 (right part). The Mach number is 0.80.

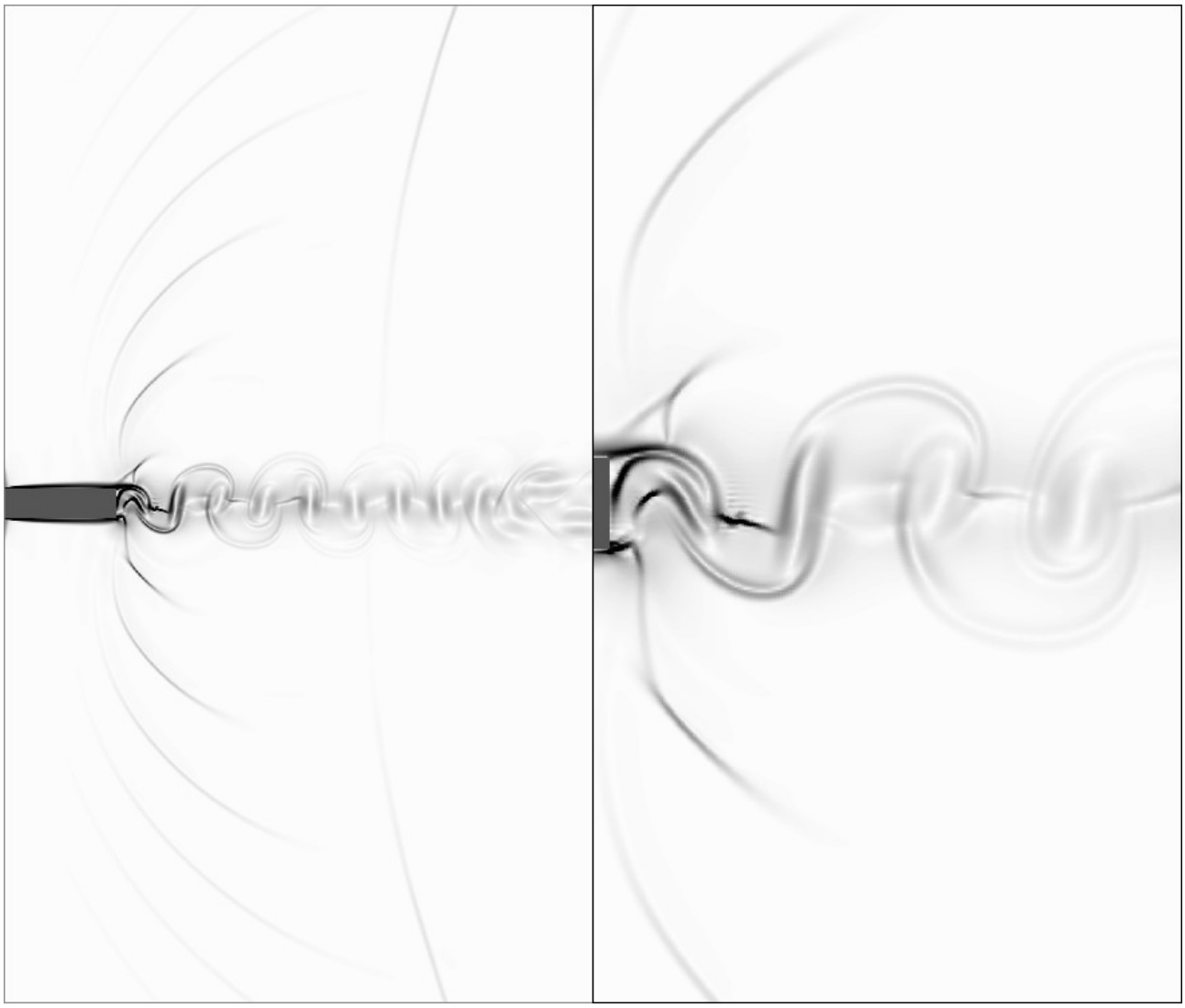

Figure 2. Visualization of the flow over the regular grid (left) with a zoom (right).

4.2. M=0.90

Figure 3 shows that the unsteady Vón Kármán vortex street is well defined and a gradual coalescence of vortices is visible from the beginning of the vortex wake. In the zoom, it is also possible to clearly see the formation of quasi-normal lambda shocks associated with the separation vortices of the upper and lower corners of the base. These quasi-normal lambda shocks bifurcate as strong acoustic waves and travel in a direction that is basically normal to the incoming flow, as the previous case, but with more intensity. In the zoom it is also possible to note that a connecting shock appears between the detached vortices as the previous case, but with more intensity, also. The intensity of this shock decreases rapidly as the vortices move in the downstream direction. The variable plotted is the nondimensional magnitude of the temperature gradient. White corresponds to 0.0 in both parts and black corresponds to 1.0 (left part) and to 2.0 (right part). The Mach number is 0.90.

Figure 3. Visualization of the flow over the regular grid (left) with a zoom (right).

4.3. M=1.00

From the visualization presented in Fig. 4 it can be seen that the unsteady Vón Kármán vortex street is well defined and, differently from the two previous cases, the coalescence of vortices is not visible. The vortex wake simply looses intensity due to viscous dissipation. In the zoom, it is also possible to clearly see the formation of oblique lambda shocks associated with the mixture layer generated by the boundary layer separation at the upper and lower corners of the base. These oblique lambda shocks continue as strong oblique shocks, produced by the coalescence of the acoustics waves. These waves also travel along the oblique shock. In the zoom it is also possible to note that the connecting shocks, that were evident in the two previous cases, are not present. The variable plotted is the nondimensional magnitude of the temperature gradient. White corresponds to 0.0 in both parts and black corresponds to 1.0 (left part) and to 2.0 (right part). The Mach number is 1.00.

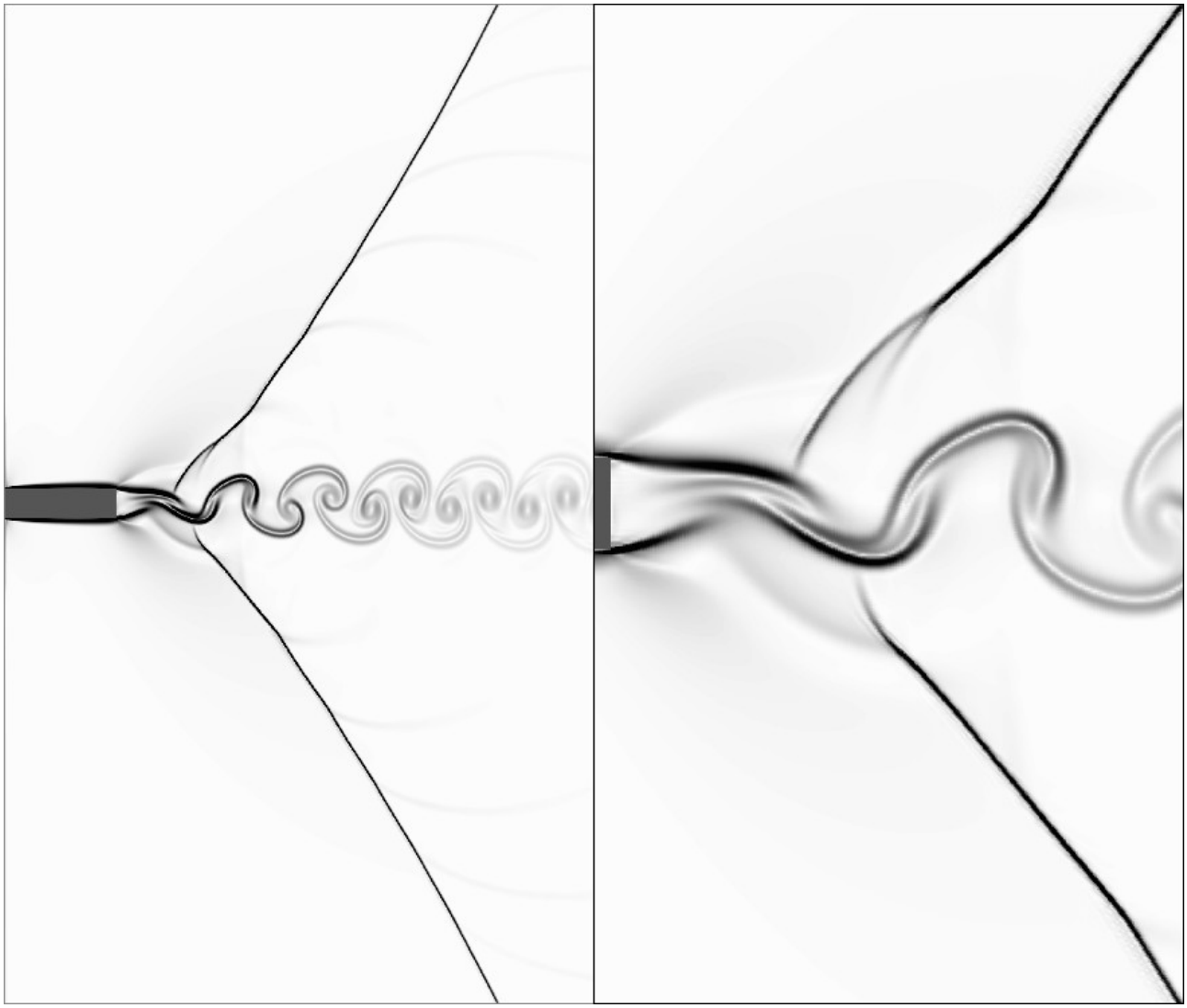

Figure 4. Visualization of the flow over the regular grid (left) with a zoom (right).

4.4. M=1.05

From the visualization presented in Fig. 5, it is evident that the buffet phenomenon is over. There is no evidence of a Vón Kármán vortex street. The boundary layer separates at the upper and lower corners and reattaches after a steady separation bubble. A compression fan is formed after separation that leads to a strong oblique shock. Since the undisturbed flow is supersonic, a weak shock (that leads to a Mach wave) is formed in the beginning of the boundary layer at the upper and lower surfaces of the base. The variable plotted is the nondimensional magnitude of the temperature gradient. White corresponds to 0.0 in both parts and black corresponds to 1.0 (left part) and to 2.0 (right part). The Mach number is 1.05.

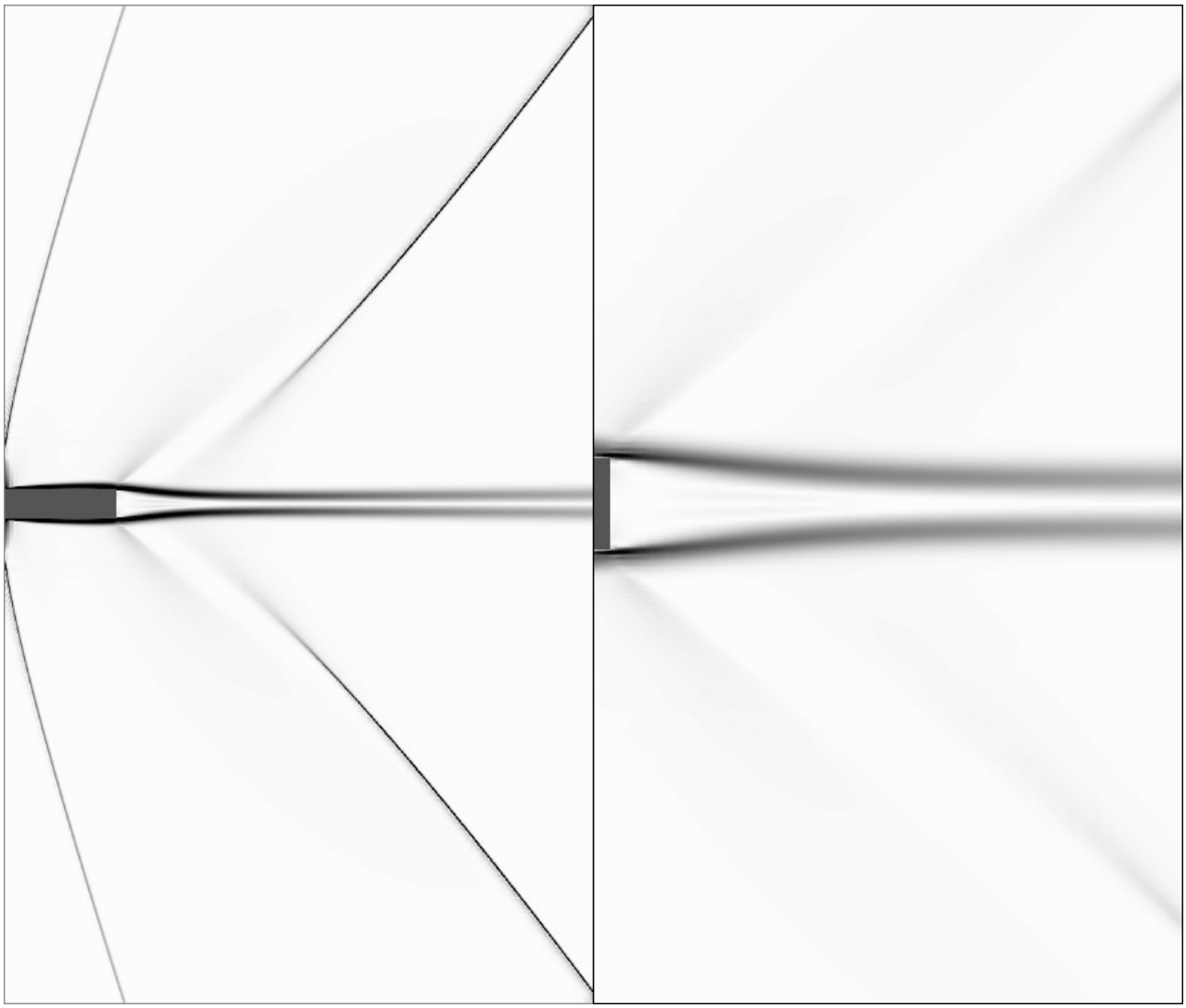

Figure 5. Visualization of the flow over the regular grid (left) with a zoom (right).

5. Conclusions

A numerical methodology, based in a finite-volume discretization, that is fourth-order accurate in space and third-order accurate in time, is proposed in order to simulate the complex vortex-shock interactions that arise in the transonic flow over a two-dimensional laminar base. The numerical results shows that a variety of very complex interactions, such as connecting shocks, oblique and quasi-normal lambda shocks and emission of strong acoustic waves can be tackled with this methodology. The results also show that the nature of these interactions is highly dependant on the Mach number. As the Mach number decreases from supersonic to subsonic, the complexity of the viscous–shock interaction increases. For subsonic Mach numbers, Fig. (2) and Fig. (3) show the emission of strong acoustic waves, in a manner similar as illustrated by Dyment (Hirsch, 1988) for the turbulent flow over a two-dimensional base. For a Mach number grater than 1.05, these interactions disappear and the transonic-buffet phenomenon for this laminar flow is over.

6. References

Anderson, D. A., Tannehill, J. C. and Pletcher, R. H., 1983, "Computational Fluid Mechanics and Heat Transfer", Hemisphe Publishing Corporation, New York, 599 p.

Daru, V., and Tenaud, C., 2001, "Evaluation of TVD high resolution schemes for unsteady viscous shocked flows", Computers and Fluids, Vol. 30, pp. 89-113.

Ducros, F., Ferrand, V., Nicoud, F., Weber, C., Darraq, D., Gacherieu, C., Poinsot, T., 1999, "Large-Eddy Simulation of the Shock/Turbulence Interaction", Journal of Computational Physics, Vol. 152, pp. 517-549.

Ducros, F., Laporte, F., Soulères, T., Guinot, V., Moinat, P. and Caruelle, B., 2000, "High-Order Fluxes for Conservative Skew-Symmetric-like Schemes in Structured Meshes: Application to Compressible Flows", Journal of Computational Physics, Vol. 161, pp. 114-139.

Hirsch, C., 1988, "Numerical Computation of Internal and External Flows", Ed. John Wiley & Sons, Chichester, 515 p.

Jameson, A., Schmidt, W. and Turkel, E., 1981, "Numerical Solutions of the Euler Equations by Finite Volume Methods Using Runge-Kutta Time-Stepping Schemes", AIAA 14th Fluid and Plasma Dynamics Conference, AIAA-81-1259, Palo Alto, California.

Sandham, N. D., Li., Q. and Yee, H. C., 2002, "Entropy Splitting for High-Order Numerical Simulation of Compressible Turbulence", Journal of Computational Physics, Vol. 178, pp. 307-322.

Yee, H. C., 1997, "Explicit and Implicit Multidimensional Compact High-Resolution Shock-Capturing Methods: Formulation", Journal of Computational Physics, Vol. 131, pp. 216-232.

Yee, H. C., Sandham, N. D. and Djomehri M. J., B., 1999, "Low-Dissipative High-Order Shock-Capturing Methods Using Characteristic-Based Filters", Journal of Computational Physics, Vol. 150, pp. 199-238.

Yee, H. C., and Sjogreen, B., 2001, "Designing Adaptive Low-Dissipative High Order Schemes for Long-Time Integration", RIACS Technical Report 01.28.

Yee, H. C., Vinokur, M. and Djomehri M. J., B., 2000, "Entropy Splitting and Numerical Dissipation", Journal of Computational Physics, Vol. 162, pp. 33-81.